

An Efficient Approach for Calibration of Automotive Radar–Camera With Real-Time Projection of Multimodal Data

Nitish Kumar^{ID}, *Graduate Student Member, IEEE*, Ayush Dasgupta^{ID}, Venkata Satyanand Mutnuri^{ID}, and Rajalakshmi Pachamuthu^{ID}, *Senior Member, IEEE*

Abstract—This article presents a comprehensive method for radar–camera calibration with a primary focus on real-time projection, addressing the critical need for precise spatial and temporal alignment between radar and camera sensor modalities. The research introduces a novel methodology for calibration utilizing geometrical transformation, incorporating radar corner reflectors to establish correspondences. This methodology applies to post-automotive manufacturing for integration into radar–camera applications such as advanced driver-assistance systems (ADASs), adaptive cruise control (ACC), collision warning, and mitigation systems. It also serves post-production for sensor installation and algorithm development. The proposed approach employs an advanced algorithm to optimize spatial and temporal synchronization and radar and camera data alignment, ensuring accuracy in multimodal sensor fusion. Rigorous validation through extensive testing demonstrates the efficiency and reliability of the proposed system. The results show that the calibration method is highly accurate compared to the existing state-of-the-art methods, with minimal errors, an average Euclidean distance (AED) of 1.447, and a root-mean-square reprojection error (RMSRE) of (0.1720, 0.5965), indicating a highly efficient spatial synchronization method. During real-time projection, the proposed algorithm for temporal synchronization achieves an average latency of 35 ms between frames.

Index Terms—Autonomous vehicles, calibration, camera, projection, radar, radar cross section (RCS), real time, reflector, robot operating system (ROS).

I. INTRODUCTION

THE advancement of autonomous driving technology has led to a surge in research on advanced driver-assistance systems (ADASs). For instance, some of the ADAS use cases include pedestrian detection, traffic sign and signal

Manuscript received 4 January 2024; revised 2 April 2024 and 29 May 2024; accepted 29 May 2024. Date of publication 3 June 2024; date of current version 12 June 2024. This work was supported by the Department of Science and Technology (DST) National Mission Interdisciplinary Cyber-Physical Systems (NM-ICPS), Technology Innovation Hub on Autonomous Navigation (TiHAN) and Data Acquisition Systems: TiHAN Foundation, Indian Institute of Technology Hyderabad (IITH). (Corresponding author: Nitish Kumar.)

Nitish Kumar and Rajalakshmi Pachamuthu are with the Department of Electrical Engineering, Indian Institute of Technology Hyderabad (IITH), Sangareddy 502284, India (e-mail: ee22mtech02005@iith.ac.in; raji@ee.iith.ac.in).

Ayush Dasgupta and Venkata Satyanand Mutnuri are with the Technology Innovation Hub on Autonomous Navigation (TiHAN) Foundation, IITH, Sangareddy 502284, India (e-mail: a.dasgupta2002@gmail.com; tihan.to2@iith.ac.in).

Digital Object Identifier 10.1109/TRS.2024.3408231

recognition, lane departure alert, lane-keeping control, and collision warning systems. Currently, cameras, light detection and ranging (LiDAR), and radio detection and ranging (radar) are the primary sensors used in the development of ADAS technologies [1], [2], [3], [4], [5]. Each sensor has its own benefits and drawbacks. Therefore, to achieve precise, robust, and reliable sensing capabilities, a heterogeneous sensor fusion system that leverages the complementary qualities of several sensors is needed. The extrinsic calibration of the camera and radar is essential for the sensor fusion of these two sensors. To effectively perform the function of multimodal sensor fusion, the calibration links the radar point clouds with the associated visual targets in a direct manner, utilizing the complementing data of heterogeneous sensors. However, in order to merge data from two or more sensors, it is critical that the data can be available in the same coordinate frame (spatial calibration) and can be gathered at the same time (temporal synchronization).

In the context of radar–camera calibration, the development of a multimodal dataset emerges as a crucial component. This dataset, comprising synchronized radar and camera data, plays a pivotal role in enhancing calibration methodologies. By aligning diverse sensor modalities, the dataset becomes a cornerstone for accurate sensor fusion and, consequently, facilitates real-time multimodal projection. The calibration process not only ensures spatial harmony between radar and camera data but also establishes the groundwork for creating robust and precisely aligned multimodal datasets.

The current state-of-the-art calibration technique predominantly revolves around extrinsic calibration. Extrinsic calibration [11], [15] of multimodal sensors, such as radar and camera, encompasses various critical steps: transforming coordinates between sensors; calibrating each sensor's intrinsic properties; determining precise mounting configurations; computing rotation and translation parameters for each axis; and formulating matrices for rotation, translation, and conversion of radar points to pixel coordinates. However, this process is both intricate and prone to errors. To mitigate these challenges, we propose a novel approach for sensor calibration where we aim to substitute the use of multiple transformations (such as translation and rotation) with a single transformation matrix. The comparison of current reprojection errors from current state-of-the-art methods is tabulated in Table I.

TABLE I
COMPARATIVE ANALYSIS WITH OTHER STATE-OF-THE-ART
METHODS IN LITERATURE

Author	Calibration Method	Sensors Used	AED	RMSE
D. Kim et al. [15]	Extrinsic	2D radar, camera	6.29	-
L. Cheng et al. [11]	Extrinsic	2D radar, camera	15.31	9.41
S. Agarwal et al. [10]	Extrinsic	2D radar, camera	- (2.2, 3.0)	
L. Cheng et al. [26]	Extrinsic	3D radar, camera	59.89	98.48
Ours	Geometric	2D radar, camera	1.47 (0.17, 0.59)	

The main contributions of this article are defined as follows.

- 1) *Spatial Synchronization:* This article introduces a novel application of geometric calibration, commonly utilized in photogrammetry, toward achieving spatial synchronization between different sensor modalities using radar and camera in automotive applications.
- 2) *Temporal Synchronization:* We propose a distinctive robot operating system (ROS)-based methodology for achieving temporal synchronization between camera and radar frames with minimum latency.
- 3) *Real-Time Implementation:* The study includes the real-time implementation of camera and radar projection, highlighting the practical application of the calibration process. The implementation demonstrates reprojection errors that are significantly lower than those observed in current state-of-the-art methodologies.

This article is organized as follows. Section II reviews multimodal sensor calibration literature. Section III examines radar behavior on reflectors. Section IV outlines the data collection method employed in this research. Section V describes the calibration methodology. Section VI explores real-time projection and application of calibration. Section VII presents the experimental results, followed by the conclusion in Section VIII.

II. LITERATURE SURVEY

The prevailing methodology for calibrating radar and camera systems entails extrinsic calibration, documented in literature such as [11], [15], [24], [25], and [26]. This method typically involves aligning the camera and radar coordinate systems with the ego-vehicle coordinate system by registering radar detections of corner reflector targets with known locations. Although akin to our approach, there are distinctions in the method employed in this article regarding reconciling of the camera and radar coordinate systems into a unified reference frame.

Several studies focus on the calibration of 3-D radar with other sensor modalities, as highlighted in [10] and [11]. However, it is important to note that calibration techniques tailored for 3-D radars may not be directly applicable to other radar types, particularly those commonly used in automotive applications which often lack elevation. In addition, the approach presented in [10] finds utility in smart roadside infrastructure,

integrating static radars, LiDARs, and cameras for dynamic object detection. In contrast, the methodology employed in this article is tailored for radars mounted on vehicles. Our approach to radar–camera calibration diverges from [11] since we leverage multiple radar reflectors for calibration purposes.

The direct linear transformation (DLT) method is a well-established mathematical approach used for geometric calibration, particularly in computer vision and photogrammetry. As outlined in [6], [7], [8], and [9], DLT serves as a concurrent resolution for transformations. Furthermore, this method directly computes solutions without necessitating preliminary approximations for the unknown parameters related to the inner and outer orientation of the camera. The core of our investigation revolves around the DLT method, enhanced through normalization and preconditioning, as a means to convert radar points to pixel coordinates seamlessly in our research. This critical calibration step is essential for achieving precise spatial alignment between radar and camera data.

Song et al. [30] and Lee et al. [31] discuss the challenges of integrating data from multiple sensors, such as radars and cameras, which have different sampling frequencies and coordinate systems. It introduced a method for time synchronization between radars and cameras using least-squares cubic spline curve fitting, which is important for combining data from different sensors. A fast spatial calibration technique based on the vehicle's longitudinal symmetry plane was also proposed, allowing for the alignment of sensor data in space. The algorithm may not account for all possible variations in vehicle designs, which could affect the spatial calibration based on the vehicle's longitudinal symmetry plane. However, the proposed method in this article presents a novel approach for calibration that works in any symmetry of the vehicle and takes care of spatial synchronization. The algorithm proposed for temporal synchronization is capable of synchronizing the sensor frames more accurately.

III. RADAR REFLECTOR ANALYSIS

A. Radar Cross Section

Radar signals encounter scattering phenomena upon interaction with uneven surfaces such as vehicles, buoys, and yachts, leading to only a fraction of signals being reflected to the radar observer. To facilitate meaningful surface reflectivity comparisons, the radar cross section (RCS) concept has been widely adopted [18], [19], [20]. Initially employed in marine operations, marine radar systems typically operate in either the X-band or S-band [27]. While larger ships utilize both bands, smaller vessels commonly rely on the X-band radar. However, it exhibits less sensitivity to smaller targets. Optimal performance in both X- and S-bands necessitates larger reflector sizes. In this article, radar applications are studied in the automotive sector. The automotive radar systems operate at 77 GHz, which is part of the millimeter-wave band (W-band) of the electromagnetic spectrum. These systems are essential for adaptive cruise control (ACC) and collision avoidance applications. This frequency range can be sensed with high resolution and operates better in various weather circumstances. Automotive radar's selection of the 77-GHz frequency achieves a balance between resolution and range,

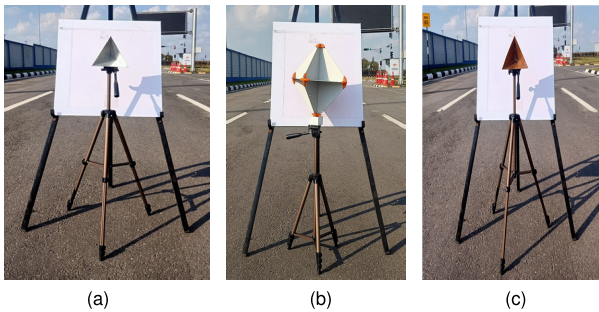


Fig. 1. Different types of radar reflectors. (a) Trihedral aluminum reflector. (b) Octahedral aluminum reflector. (c) Trihedral copper reflector.

making it ideal for guaranteeing safety in various driving conditions.

B. Radar Target Design Analysis

From the standard available radar reflectors, as discussed in [21], our analysis is mainly on the reflector's size, shape, and material. Typically, a complex target's RCS is calculated by logically integrating the cross sections of the simple forms that comprise it. A collection of distinct scattering centers dispersed throughout the target can be used to model a complicated target RCS, as discussed in [21].

Three types of radar reflectors were analyzed for this research, as shown in Fig. 1(a)–(c) containing trihedral aluminum reflector, octahedral aluminum reflector, and trihedral copper reflector, respectively.

The trihedral aluminum reflector is a traditional choice known for its simplicity and effectiveness. This reflector is designed with an edge length of 15.24 cm. Its triangular shape facilitates the efficient reflection of radar signals back toward the source. The RCS values of the aluminum corner reflector are examined to understand its performance in the context of radar point data collection.

The octahedral aluminum reflector introduces a geometric variation to the traditional corner reflector. This octahedral reflector has an edge length of 20.32 cm. The additional surfaces may influence the RCS values, and this study aims to assess the impact of such modifications on radar reflection efficiency.

Copper, a good electrical conductor, is introduced as a reflective material to evaluate its suitability for radar reflection analysis. The trihedral copper reflector provides an alternative perspective, considering the impact of material conductivity on RCS values. This corner reflector design is the same as a trihedral aluminum reflector with an edge length of 15.24 cm.

C. Comparative Analysis and Results

The comparative analysis involves measuring and comparing the RCS values of each reflector type. The experiment is performed using ARS430DI Continental long-range radar and with the above three different types of reflectors. The goal is to conduct a comparative analysis of RCS values obtained from the radar when each reflector is placed at variable distances. The experimental configuration entailed sequentially positioning each reflector in front of the radar, one at a time,

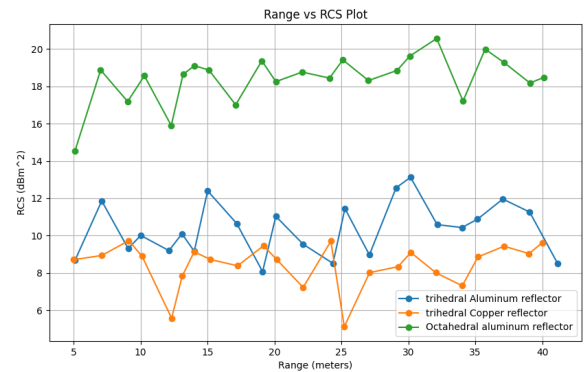


Fig. 2. Radar reflector analysis.

at distances ranging from 5 to 40 m. At each distance, the radar system recorded the range and RCS values, representing the reflectivity of the corner reflectors at variable distances. This process was repeated for each reflector type to gather comprehensive data for analysis. This analysis is instrumental in understanding the efficiency of each reflector type in radar point data collection. From the graph in Fig. 2, it has been observed that the RCS values of the octahedral aluminum reflector are higher than those of the other two reflectors. Also, the copper reflector's reflectivity is very close to the aluminum corner reflector's reflectivity. Hence, it can be concluded that copper, being a good conductor, can also be used for radar reflectors with traditional aluminum reflectors. Also, the higher the size of the reflector, the more RCS property the material will have. This analysis was performed to refine the reflector types and proceed with an appropriate type of reflector for further research purposes. After this experiment, we performed all our calibration methodologies using octahedral aluminum reflectors and trihedral aluminum reflectors. Ultimately, the findings will contribute to refining calibration methodologies and enhancing the precision and reliability of autonomous vehicle perception systems.

IV. DATA COLLECTION FOR CALIBRATION

A critical step to enhance the accuracy of perception systems in autonomous vehicles involves the meticulous collection of data for radar camera calibration. The calibration process aims to synchronize radar and camera systems, ensuring multimodal sensor data fusion. This section outlines the methodology employed for data collection, emphasizing the utilization of reflectors to establish correspondences between radar reflections and camera pixels.

For data recording, the ARS430DI long-range radar, a web-camera, and a Basler camera were utilized. The long-range radar features two modes of detection: a far-range scan spanning from 0.2 to 200 m with $\pm 9^\circ$ azimuth coverage and a near-range scan ranging from 0.2 to 100 m with $\pm 60^\circ$ azimuth coverage. The range accuracy is specified at 0.1 m, with a range resolution of 0.39 m. In addition, the azimuth beamwidth measures 2.2° with an accuracy of 0.1° and a resolution of 1.6° . An embedded DSP processor is integrated, facilitating the separation of range and azimuth values. The radar data comprise point cloud data with a comprehensive set of parameters, including range, azimuth, relative velocity, RCS, false

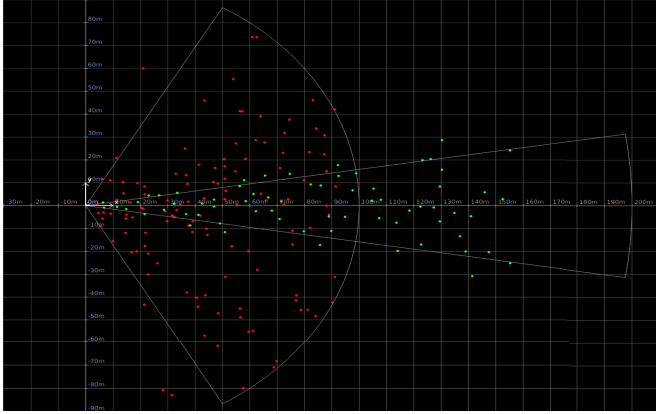


Fig. 3. Radar point cloud data visualization (red points are from the near scan and green points are from the far scan).

alarm indicator flags, and signal-to-noise ratio (SNR) values. Fig. 3 shows the radar point clouds from the ARS430 radar sensor.

Trihedral aluminum reflectors were chosen as the calibration object to facilitate the calibration process. The reflective behavior of the reflector aids in establishing clear correspondences between radar detections and their corresponding camera pixels, forming the basis for accurate calibration. Data collection was carried out in multiple iterations, each involving the placement of the reflectors at varying distances ranging from 5 to 40 m and at multiple azimuths from -40° to 40° from the sensor suite. Multiple distances are used to allow the calibration algorithm to account for signal characteristics and sensor perspective changes across different operational scenarios. The data were captured under static conditions using an ROS-based platform, ensuring time-synchronized data streams from radar and cameras. For each iteration, the radar system records the reflected signals from the aluminum reflector. Simultaneously, the corresponding camera captures images of the reflective object within its field of view. Fig. 4 shows the corner reflector in the camera image and their corresponding radar points. The whiteboard behind the marker is kept to identify the marker's position by the camera at larger distances. In the postprocessing of data, the radar detections containing the reflector's range, RCS, azimuth, and coordinate information were extracted. The corresponding camera pixel information of the reflector was determined manually from the synchronized camera image using the OpenCV [23] image visualizer. This one-to-one correspondence of radar–camera data was stored for spatial calibration. The data collection process was iterative, with each iteration refining the dataset and contributing to the robustness of the calibration algorithm. This iterative approach is crucial for capturing nuances in sensor behavior and optimizing the calibration parameters across a spectrum of distances.

V. CALIBRATION METHODOLOGY

In this article, the calibration of radar and camera is performed using geometric transformation, as discussed in [7] and [22], employing DLT but in a more analytical manner. The existing state-of-the-art DLT method converts the world

coordinates into camera coordinates of a single modality. In this article, multimodal data, that is, point clouds from radar and images from the camera, were used to transform points from radar dimension to camera pixels. Normalization of DLT was done, and the results were optimized to obtain better results. This is discussed in detail in this section.

The radar–camera sensors were calibrated by collecting a set of more than 120 radar–camera data pairs at different ranges and azimuths in front of the vehicle in multiple iterations, as explained in Section IV. Let $\{\mathbf{R}_i = [x_i, y_i, z_i]^T\}_{i=1}^K$ and $\{\mathbf{C}_i = [u_i, v_i]^T\}_{i=1}^K$ denote K sets of radar and camera pairs, respectively. This calibration aimed to estimate a 3-D projection transformation matrix that converts the radar data into a 2-D image. The radar–camera data pairs are related as

$$\bar{\mathbf{C}} = \mathbf{M}\bar{\mathbf{R}} \quad (1)$$

where $\bar{\mathbf{R}}$ and $\bar{\mathbf{C}}$ are the homogeneous coordinates of \mathbf{R} and \mathbf{C} , respectively, and \mathbf{M} is the transformation matrix denoted as $\mathbf{M} = [m_{ij}]_{3 \times 4}$.

Before applying the geometric transformation, a preconditioning or normalization method was applied to radar and image points. The preconditioning involves manipulating the input data to ensure optimal numerical properties for subsequent computational procedures. Here, this process typically performs centering and scaling of image and radar coordinates. The centering feature, achieved by subtracting the mean of the coordinates, helps avoid potential numerical precision issues by placing the data around the origin. The scaling feature ensures that the data fall within an appropriate range, guarding against numerical instabilities that arise from extreme values. The centering and scaling procedures are mathematically expressed as

$$\tilde{\mathbf{R}}_i = \mathbf{T}_r \bar{\mathbf{R}}_i = \begin{bmatrix} l_1 & 0 & 0 & -l_1\mu_1 \\ 0 & l_1 & 0 & -l_1\mu_2 \\ 0 & 0 & l_1 & -l_1\mu_3 \\ 0 & 0 & 0 & 1 \end{bmatrix} \bar{\mathbf{R}}_i \quad (2)$$

$$\tilde{\mathbf{C}}_i = \mathbf{T}_c \bar{\mathbf{C}}_i = \begin{bmatrix} l_2 & 0 & -l_2\eta_1 \\ 0 & l_2 & -l_2\eta_2 \\ 0 & 0 & 1 \end{bmatrix} \bar{\mathbf{C}}_i. \quad (3)$$

Here, consider \mathbf{T}_r as the normalized matrix corresponding to $\bar{\mathbf{R}}$ and \mathbf{T}_c as the normalized matrix corresponding to $\bar{\mathbf{C}}$. These matrices can be employed and expressed in (2) and (3), where $\mu_1\text{--}\mu_3$ are the elements of mean vector for radar denoted as in (4) and η_1 and η_2 are the elements of mean vector for camera denoted as in (5)

$$\boldsymbol{\mu} = \frac{\sum_{i=1}^K \mathbf{R}_i}{K} \quad (4)$$

$$\boldsymbol{\eta} = \frac{\sum_{i=1}^K \mathbf{C}_i}{K}. \quad (5)$$

l_1 and l_2 are the norms average of $\sqrt{2}/\{\mathbf{R}_i - \boldsymbol{\mu}\}_{i=1}^K$ and $\sqrt{2}/\{\mathbf{C}_i - \boldsymbol{\eta}\}_{i=1}^K$, respectively. After applying the above preconditioning and normalization method, we obtain $\tilde{\mathbf{R}}_i$ and $\tilde{\mathbf{C}}_i$ for radar and camera points, respectively. Proceeding with geometric transformations, applying preconditioning in (1), the

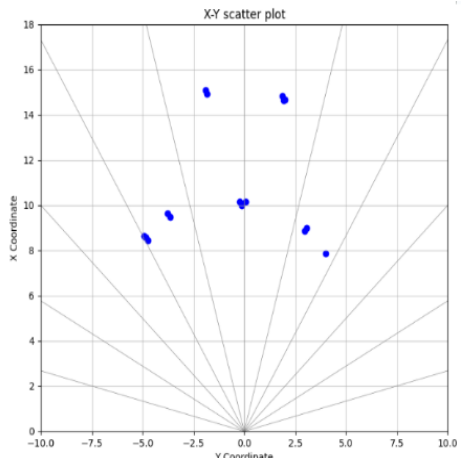


Fig. 4. Radar reflector points from radar and corresponding reflectors in the camera frame.

equations are obtained as

$$\begin{bmatrix} u_i \\ v_i \\ 1 \end{bmatrix} = \begin{bmatrix} u_i w \\ v_i w \\ w \end{bmatrix} = \begin{bmatrix} m_{11} & m_{12} & m_{13} & m_{14} \\ m_{21} & m_{22} & m_{23} & m_{24} \\ m_{31} & m_{32} & m_{33} & m_{34} \end{bmatrix} \begin{bmatrix} X_i \\ Y_i \\ Z_i \\ 1 \end{bmatrix} \quad (6)$$

where w is a scaling factor. Upon solving (6), the formulas for u_i and v_i are obtained as shown in the following equations:

$$u_i = \frac{m_{11}X_i + m_{12}Y_i + m_{13}Z_i + m_{14}}{m_{31}X_i + m_{32}Y_i + m_{33}Z_i + m_{34}} \quad (7)$$

$$v_i = \frac{m_{21}X_i + m_{22}Y_i + m_{23}Z_i + m_{24}}{m_{31}X_i + m_{32}Y_i + m_{33}Z_i + m_{34}}. \quad (8)$$

Equations (7) and (8) can be further solved to obtain a set of homogeneous systems of linear equations, as shown in the following equations:

$$\begin{aligned} u_i m_{31}X_i + u_i m_{32}Y_i + u_i m_{33}Z_i + u_i m_{34} \\ - m_{11}X_i - m_{12}Y_i - m_{13}Z_i - m_{14} = 0 \end{aligned} \quad (9)$$

$$\begin{aligned} v_i m_{31}X_i + v_i m_{32}Y_i + v_i m_{33}Z_i + v_i m_{34} \\ - m_{21}X_i - m_{22}Y_i - m_{23}Z_i - m_{24} = 0. \end{aligned} \quad (10)$$

Hence, (9) and (10) can be represented in the equation of the form $\mathbf{A}\vec{\mathbf{m}} = \mathbf{0}$ where

$$\mathbf{A} = \begin{bmatrix} X_i & Y_i & Z_i & 1 & 0 & 0 & 0 & 0 & -u_i X_i & -u_i Y_i & -u_i Z_i & -u_i \\ 0 & 0 & 0 & 0 & X_i & Y_i & Z_i & 1 & -v_i X_i & -v_i Y_i & -v_i Z_i & -v_i \end{bmatrix} \quad (11)$$

and $\vec{\mathbf{m}}$ is the flattened vector matrix containing elements of \mathbf{M} and $\mathbf{m} = [m_{11}, m_{12}, m_{13}, \dots, m_{33}, m_{34}]^T$. The objective of this experiment is to solve this homogeneous system, which is equivalent to determining the coefficients of matrix \mathbf{M} . Currently, each homogeneous system has a trivial solution, referred to as the zero solution, which can be reached by giving each element a value of zero. The exact answer has not yet been found. An approximation could be attempted, assuming that one exists.

From a mathematical perspective, this means that rather than trying to solve $\mathbf{A}\vec{\mathbf{m}} = \mathbf{0}$ exactly, $\vec{\mathbf{m}}$ was chosen such that $|\mathbf{A}\vec{\mathbf{m}}|$ is minimized. In essence, the goal was to reduce the

algebraic error in this case. In addition, $\vec{\mathbf{m}}$ can be normalized to turn it into a unit vector. Matrix \mathbf{M} is a scale-invariant matrix; it does not change if scales of length or other variables are multiplied by a common factor, so it can be normalized by selecting a scale factor equal to the magnitude. Now, the minimum value of $|\mathbf{A}\vec{\mathbf{m}}|$ needs to be found, constrained to $|\vec{\mathbf{m}}| = 1$. It is known that if the unit vector $\vec{\mathbf{m}}$ is along the smallest eigenvector of $\mathbf{A}^T \mathbf{A}$, then $|\mathbf{A}\vec{\mathbf{m}}|$ will be minimized.

Considering k set of pairs of radar and camera, matrix \mathbf{A} will have dimension $2k \times 12$ and can be expanded as shown in (12), bottom of the next page.

The idea is to locate certain spots in the radar coordinate denoted by $\{X_i, Y_i, Z_i\}$, locate the projections of those points in the image denoted by $\{u_i, v_i\}$, and then compute matrix \mathbf{A} . The labeling procedure at the camera side was done manually. The form of the matrix \mathbf{A} will now be $2k \times 12$ when k points are labeled, but the shape of $\vec{\mathbf{m}}$ remains fixed at 12×1 . Since the size of $\vec{\mathbf{m}}$ is 12, there are 12 unknowns. To identify these 12 unknowns, 12 separate equations need to be solved. In order to solve for $\vec{\mathbf{m}}$, at least six independent points must be labeled, which means that k must be at least 6. More points could be labeled as well; the more points, the better the result, but six is the least, and no three points should be collinear.

Thus, to construct matrix \mathbf{A} , at least six pairs of camera–radar points are found. After that, $\mathbf{A}^T \mathbf{A}$ is computed, and the eigenvector with the lowest eigenvalue yields $\vec{\mathbf{m}}$. The vector $\vec{\mathbf{m}}$ is then reshaped to the 3×4 matrix \mathbf{M} , which serves as our final calibration matrix.

A. Optimization Process

In the calibration process that we discussed above, the goal was to find the value of $\vec{\mathbf{m}}$ that would fit nicely into the algebraic equation $\mathbf{A}\vec{\mathbf{m}} = \mathbf{0}$ in order to minimize the algebraic error. The algorithm may encounter problems when nonlinear errors and uncertainties, such as radial distortion, enter the camera, as they frequently do in the actual world. For this reason, optimization should be performed for the appropriate type of error. The geometric error is the one that should be examined. Geometric error provides an approximation of the deviation between the expectations and the actual data.

It accomplishes this by calculating the difference between a point's ground truth projection and its expected projection. Here, the gap between the predictions and the actual data was decreased while minimizing the geometric error. Ground truth data are the camera pixel points of the radar reflector from an image that is collected manually, as discussed in Section IV, and predictions are the 2-D points obtained after multiplying radar detections with 3×4 matrix \mathbf{M} . The geometric error is given by

$$e = \sum_{i=1}^k d(\mathbf{C}_i, \mathbf{MR}_i) \quad (13)$$

where e is the geometric error, d is the distance metric function, \mathbf{M} is the calibration matrix obtained in Section V, \mathbf{C}_i is the ground truth projection of X_i from camera, and \mathbf{R}_i is the radar detection points corresponding to \mathbf{C}_i . Therefore, the goal is to minimize the geometric error by updating the weights of matrix M and doing a nonlinear optimization. For the optimization process, optimization algorithms in the `scipy.optimize` [28] python module were utilized.

The function `minimize` from the module `scipy.optimize` takes in two important arguments: the error function and the initial weights. The geometric error from (13) was passed as the first argument, and the 12-D vector $\vec{\mathbf{m}}$ was passed as the second argument as the initial state. The optimization procedure is carried out and completed after executing the `minimize` function; the returned result is a 12-D weight vector, which is then reshaped into a 3×4 matrix, which is finally used to compute the predictions. The overall flow diagram of the calibration methodology was mentioned in Fig. 5.

VI. REAL-TIME MULTIMODAL PROJECTION OF RADAR ON CAMERA

Spatial and temporal synchronization is a critical consideration in achieving real-time projection of radar data onto camera frames for subsequent radar-camera sensor fusion. Spatial synchronization is already achieved in Sections IV and V using calibration. The ROS platform, on the other hand, is instrumental in addressing the challenge of temporal synchronization. The details of the algorithm are explained as follows. It provides a robust framework for managing the temporal aspects of sensor data, ensuring precise synchronization between radar and camera feeds. Upon successful implementation of temporal synchronization through ROS, a foundation is established for enhancing the accuracy and reliability of radar-camera sensor fusion in real-time applications,

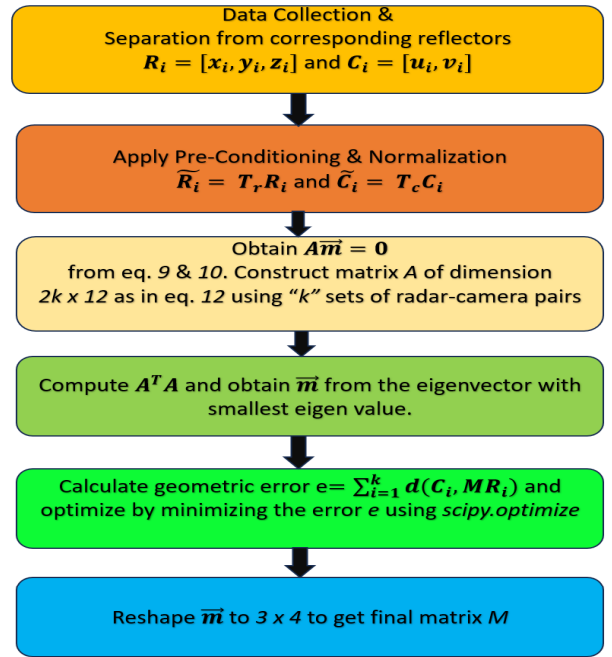


Fig. 5. Flow of the calibration methodology.

contributing to the advancement of autonomous systems and their perception capabilities.

The ARS430DI radar operates at a frame rate of 27.77 Hz, covering both near- and far-range scans, while the camera exhibits a varying frame rate ranging from 15 to 20 Hz. To harmonize these disparate frequencies, radar and camera data of each timestamp are published through distinct ROS topics to a shared platform. Temporal synchronization is achieved through the application of the algorithm outlined in Algorithm 1, ensuring a seamless coordination of data streams. The steps and flow required for real-time projection are shown in Fig. 6.

Post-synchronization, the closest radar points corresponding to the timestamp of the camera image are extracted, effectively discarding extraneous radar data. This curation is essential due to the disparate frequencies between the radar and camera systems, allowing for optimal real-time temporal synchronization. Fig. 7 represents the time delay or latency between each synchronized radar-camera respective frames in real time. It has been observed that there is an average delay of approximately 35 ms between each radar camera frame, with a minimum latency of 53 ms and a maximum latency of 77 ms.

$$A = \begin{bmatrix} X_1 & Y_1 & Z_1 & 1 & 0 & 0 & 0 & 0 & -u_1 X_1 & -u_1 Y_1 & -u_1 Z_1 & -u_1 \\ 0 & 0 & 0 & 0 & X_1 & Y_1 & Z_1 & 1 & -v_1 X_1 & -v_1 Y_1 & -v_1 Z_1 & -v_1 \\ X_2 & Y_2 & Z_2 & 1 & 0 & 0 & 0 & 0 & -u_2 X_2 & -u_2 Y_2 & -u_2 Z_2 & -u_2 \\ 0 & 0 & 0 & 0 & X_2 & Y_2 & Z_2 & 1 & -v_2 X_2 & -v_2 Y_2 & -v_2 Z_2 & -v_2 \\ & & & & \dots \\ & & & & \dots \\ X_k & Y_k & Z_k & 1 & 0 & 0 & 0 & 0 & -u_k X_k & -u_k Y_k & -u_k Z_k & -u_k \\ 0 & 0 & 0 & 0 & X_k & Y_k & Z_k & 1 & -v_k X_k & -v_k Y_k & -v_k Z_k & -v_k \end{bmatrix} \quad (12)$$

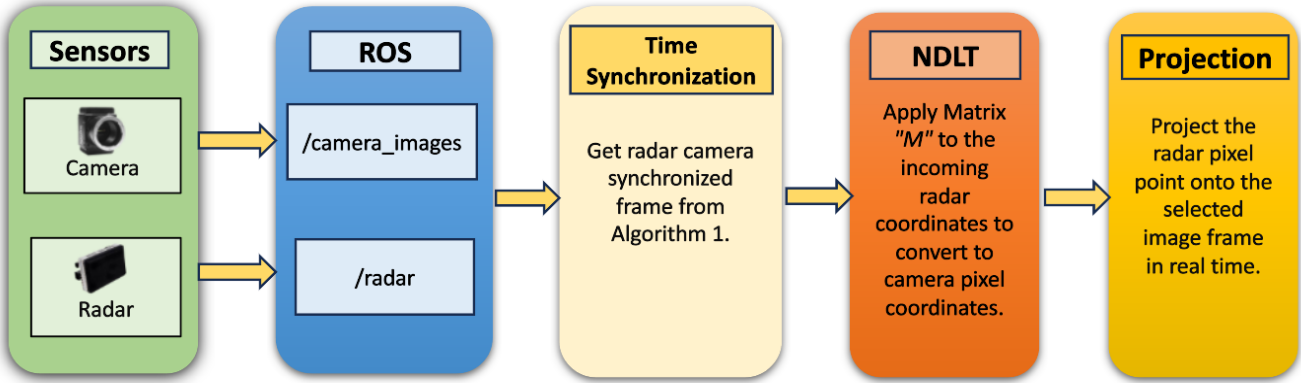


Fig. 6. Flow diagram for radar–camera real-time projection.

Algorithm 1 Radar–Camera Time Synchronization

```

Step 1: Declare two arrays  $P[]$  and  $Q[]$  and initialize  $i = 0$  and  $j = 0$ .
Step 2: Receive radar data continuously from  $/radar$  ROS topic and store it in  $P[j]$  with timestamps.
Step 3: Receive camera data continuously from  $/camera\_images$  ROS topic and store each frame in  $Q[j]$  with timestamps.
Step 4:
if  $Q[i] == 0$  then
    Increment  $j \rightarrow j + 1$ 
    goto Step 2
else
    Select radar data from  $P[j]$ ,  $P[j - 1]$  and camera image from  $Q[i]$  with their respective timestamps.
end if
Step 5: Perform the absolute difference between camera timestamp and radar timestamps and store it in  $t_1$  and  $t_2$ , respectively.

$$t_1 = |Q[i] - P[j]| \text{ and } t_2 = |Q[i] - P[j - 1]|$$

Step 6:
if  $t_1 \geq t_2$  then
    Radar data of  $P[j - 1]$  and camera image of  $Q[i]$  are synchronized data.
    Increment  $i \rightarrow i + 1$ 
    goto Step 2
else
    Radar data of  $P[j]$  and camera image of  $Q[i]$  are synchronized data.
    Increment  $i \rightarrow i + 1$ 
    goto Step 2
end if

```

The utilization of the matrix M from (16) facilitates the real-time spatial synchronization of radar and camera data. This synchronization helps in producing radar-projected data onto camera images in real time. The integration of these synchronized datasets serves as a fundamental advancement in the multimodal fusion of radar–camera information, promising heightened accuracy and reliability in real-time applications.

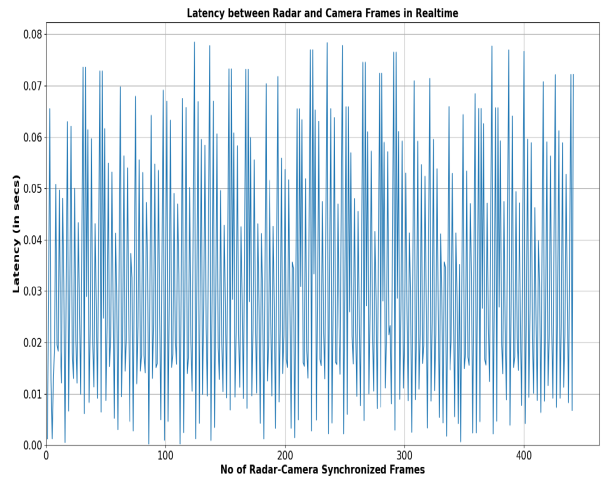


Fig. 7. Latency analysis after getting synchronized radar and camera frames from ROS.

VII. RESULTS AND EXPERIMENTS

In the calibration process, ARS430DI Continental long-range radar, FINGERS 1080 Hi-Res USB Webcam, and Basler acA1920-40gc camera were used. The radar sensor is installed in the vehicle's front end, and the camera is installed at the top, as shown in Fig. 8. With these sensors on board, data collection was started from both radar and camera sensors, and the postprocessing of data was performed as discussed in Section IV. The image's resolution was set at 640×480 pixels. If the corner reflectors are positioned far from the camera, they become imperceptible since their absolute sizes are inadequate. A piece of white hardboard and corner reflectors were utilized to address this issue. The data collection process was performed by keeping at least seven sets of corner reflectors in front of the vehicles at different positions. This process was carried out multiple times and at various distances using the ROS platform to ensure data synchronization.

After manually associating the radar data with its corresponding camera pixel coordinate, as discussed in Section IV, the data were divided into training and testing data pairs in the ratio 2:1, respectively. At every iteration, the training data pairs

TABLE II
AED AND RMSRE COMPARISON ANALYSIS OF DLT AND NDLT FOR DIFFERENT VALUES OF K

	Average Euclidean Distance (AED)																	
	K (12)		K (18)		K (21)		K (27)		K (36)		K (42)		K (51)		K (57)		K (63)	
DLT	7.4732		4.6925		3.5395		2.6836		2.2876		2.3108		1.9676		1.7732		1.6228	
NDLT	3.6554		3.1129		2.8667		2.2751		1.9815		2.0365		1.7441		1.4809		1.4774	
Root Mean Square Re-projection Error (RMSRE) for (u, v)																		
	u	v	u	v	u	v	u	v	u	v	u	v	u	v	u	v		
DLT	2.127	6.698	3.461	0.811	3.1149	0.1180	1.9992	1.0732	2.0133	0.4450	1.887	0.9432	1.6126	0.7957	1.4168	0.7414	1.3131	0.6474
NDLT	3.3951	0.7759	2.9282	0.603	2.2685	1.1332	1.9754	0.3033	1.7631	0.5993	1.6381	0.8851	1.2066	1.0157	1.239	0.6160	0.1720	0.5965



Fig. 8. Radar and camera sensors mounted on the vehicle platform.

were ensured to be at least six in number, and it was increased in further trials to get the correct calibration matrix. The above experiment was performed with and without applying normalization and preconditioning to the DLT method, and the results were compared. To create a numerical comparison between DLT and normalized DLT (NDLT), the calibration error for K pairs of $\{R_i\}$ and $\{C_i\}$, which is the average Euclidean distance (AED) between ground truths and predictions, was utilized as in the following equation:

$$E_d = \frac{1}{K} \sum \| \widehat{C}_i, C_i \| \quad (14)$$

where \widehat{C}_i is the predictions of radar coordinate mapped from $\{R_i\}$. The root-mean-square reprojection error (RMSRE) was calculated by calculating the pixel errors between the original camera pixels and its predicted radar points' pixel coordinates as shown in the following equation:

$$\text{Err}_{\text{rms}} = \sqrt{\frac{1}{K} \sum_{i=1}^K \| C_i - R_i \|_2^2} \quad (15)$$

where C_i contains the ground truth pixel values (u, v) and R_i contains the predicted radar points in pixel coordinates (u', v') .

Also, after normalization (NDLT), a significant improvement in performance was observed. Fig. 9 shows the projection of one set of predicted radar points to ground truth camera

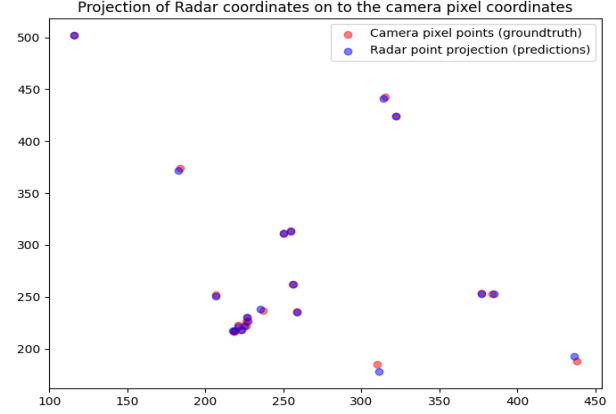


Fig. 9. Projection of radar points to camera pixel coordinates after optimization in NDLT.

pixel coordinates for $K = 21$ points. Red dots denote the camera pixel points $\{u, v\}$ of the corner reflector from the image, and blue dots represent the converted radar points to pixel coordinates using NDLT. It can be seen that the predicted radar pixel points closely match the ground truth camera pixel coordinates, and the corresponding RMSRE was (2.2685, 1.1332). After optimization, the AED and RMSRE for different values of radar-camera pairs (K) were tabulated in Table II and the plot of AED for different values of K was plotted in Fig. 10. It has been observed from the table and the plot that as we increase the number of radar-camera data pairs (K), the distance error reduces significantly. After performing calibration and optimization, we obtain the final 3×4 matrix M as shown in (16). This matrix is further used for performing radar-camera projection in real time

$$M = \begin{bmatrix} -24.70429 & 37.46050 & -21.82521 & -27.98080 \\ -15.89052 & 63.73530 & -39.19509 & -50.25022 \\ -0.0804 & 0.00188 & -0.59391 & 0.31224 \end{bmatrix}. \quad (16)$$

In the real-time projection of radar data onto camera frames, integrating the YOLOv8 model for object detection in camera images significantly enhances the system's capabilities. Following the projection, a filtering step is implemented to

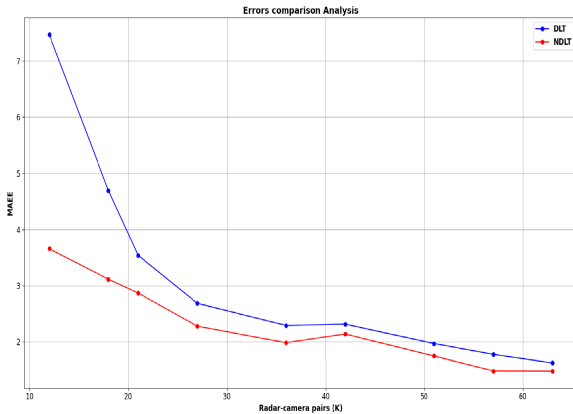


Fig. 10. AED comparison analysis for DLT and NDLT.



Fig. 11. Real-time projection of radar points on the camera images. (a)–(c) Person's detection at different positions. (d)–(f) Detection of a vehicle at different positions.

selectively retain radar points associated with detected objects in the camera frames. Leveraging the bounding box information generated by YOLOv8, unwanted radar projections are effectively filtered out, ensuring that only radar points corresponding to objects of interest are retained for further analysis. This integrated approach not only facilitates the alignment of radar and camera data but also refines the multimodal dataset by eliminating extraneous radar projections, ultimately contributing to the accuracy and reliability of object association in the context of multimodal sensor fusion. From Fig. 11, depicting real-time projections of radar onto camera frames, a notable consistency emerges as the radar detections consistently align precisely within the bounding boxes encompassing persons and vehicles at various positions. The seamless alignment of radar points within the designated bounding boxes suggests robust object association, affirming the accuracy and reliability of the multimodal sensor fusion methodology. This integration not only showcases the system's capability to project radar data onto corresponding camera frames accurately but also highlights its versatility in capturing objects of distinct shapes and sizes across varying spatial positions. The successful co-localization of radar detections within the predefined bounding boxes presents a promising

foundation for further advancements in real-time object detection and tracking within the context of autonomous systems.

VIII. CONCLUSION

The comprehensive exploration of the radar–camera calibration process and real-time projection has provided valuable insights into the details of multimodal sensor fusion methodologies for autonomous systems. Through the evaluation of three distinct radar corner reflectors—the trihedral aluminum, octahedral aluminum, and trihedral copper reflectors—it was determined that the octahedral aluminum reflector exhibited superior performance in the calibration process. The calibration procedure employing the DLT technique with normalization and preconditioning demonstrated its efficacy in converting radar points to pixel coordinates, ensuring accurate spatial alignment between radar and camera data.

The seamless transition from calibration to real-time projection showcased the practical implications of this research. The successful integration of radar points onto camera frames in real time, with a focus on object association and precise localization within bounding boxes, is a testament to the robustness and reliability of the proposed multimodal sensor fusion approach. This study not only establishes the importance of selecting an optimal reflector for radar calibration but also emphasizes the significance of employing sophisticated calibration techniques for accurate sensor fusion. The results presented herein lay a solid foundation for further research in refining and advancing radar–camera integration, offering promising avenues for enhancing the precision and reliability of perception systems in autonomous applications.

ACKNOWLEDGMENT

All the experiments are performed at the TiHAN testbed [29] and TiHAN test track [32].

REFERENCES

- [1] Y. Wang, G. Wang, H.-M. Hsu, H. Liu, and J.-N. Hwang, "Rethinking of radar's role: A camera-radar dataset and systematic annotator via coordinate alignment," in *Proc. IEEE/CVF Conf. Comput. Vis. Pattern Recognit. Workshops (CVPRW)*, Jun. 2021, pp. 2815–2824.
- [2] Z. Liu et al., "Robust target recognition and tracking of self-driving cars with radar and camera information fusion under severe weather conditions," *IEEE Trans. Intell. Transp. Syst.*, vol. 23, no. 7, pp. 6640–6653, Jul. 2022, doi: [10.1109/TITS.2021.3059674](https://doi.org/10.1109/TITS.2021.3059674).
- [3] D. J. Yeong, G. Velasco-Hernandez, J. Barry, and J. Walsh, "Sensor and sensor fusion technology in autonomous vehicles: A review," *Sensors*, vol. 21, no. 6, p. 2140, Mar. 2021.
- [4] Y. Xiao, F. Codevilla, A. Gurram, O. Urfalioglu, and A. M. López, "Multimodal end-to-end autonomous driving," *IEEE Trans. Intell. Transp. Syst.*, vol. 23, no. 1, pp. 537–547, Jan. 2022.
- [5] H. Cho, Y.-W. Seo, B. V. K. V. Kumar, and R. R. Rajkumar, "A multi-sensor fusion system for moving object detection and tracking in urban driving environments," in *Proc. IEEE Int. Conf. Robot. Autom. (ICRA)*, May 2014, pp. 1836–1843.
- [6] Y. I. Abdel-Aziz, H. M. Karara, and M. Hauck, "Direct linear transformation from comparator coordinates into object space coordinates in close-range photogrammetry," *Photogramm. Eng. Remote Sens.*, vol. 81, no. 2, pp. 103–107, 2015, doi: [10.14358/PERS.81.2.103](https://doi.org/10.14358/PERS.81.2.103).
- [7] R. Hartley and A. Zisserman, *Multiple View Geometry in Computer Vision*, 2nd ed. New York, NY, USA: Cambridge Univ. Press, 2003.
- [8] K. Huang, S. Ziauddin, M. Zand, and M. Greenspan, "One shot radial distortion correction by direct linear transformation," in *Proc. IEEE Int. Conf. Image Process. (ICIP)*, Abu Dhabi, United Arab Emirates, Oct. 2020, pp. 473–477, doi: [10.1109/ICIP40778.2020.9190749](https://doi.org/10.1109/ICIP40778.2020.9190749).

- [9] G. Wang, J. Li, P. Zhang, X. Zhang, and H. Song, "Pedestrian speed estimation based on direct linear transformation calibration," in *Proc. Int. Conf. Audio, Lang. Image Process.*, Shanghai, China, Jul. 2014, pp. 195–199, doi: [10.1109/ICALIP.2014.7009785](https://doi.org/10.1109/ICALIP.2014.7009785).
- [10] S. Agrawal, S. Bhandari, K. Doycheva, and G. Elger, "Static multitarget-based autocalibration of RGB cameras, 3-D radar, and 3-D LiDAR sensors," *IEEE Sensors J.*, vol. 23, no. 18, pp. 21493–21505, Sep. 2023.
- [11] L. Cheng, A. Sengupta, and S. Cao, "3D radar and camera co-calibration: A flexible and accurate method for target-based extrinsic calibration," in *Proc. IEEE Radar Conf. (RadarConf23)*, San Antonio, TX, USA, May 2023, pp. 1–6.
- [12] G. Yan, F. He, C. Shi, X. Cai, and Y. Li, "Joint camera intrinsic and LiDAR-camera extrinsic calibration," 2022, *arXiv:2202.13708*.
- [13] P. An et al., "Geometric calibration for LiDAR-camera system fusing 3D–2D and 3D–3D point correspondences," *Opt. Exp.*, vol. 28, no. 2, pp. 2122–2141, 2020.
- [14] C. Song, G. Son, H. Kim, D. Gu, J.-H. Lee, and Y. Kim, "A novel method of spatial calibration for camera and 2D radar based on registration," in *Proc. 6th IIAI Int. Congr. Adv. Appl. Informat. (IIAI-AAI)*, Jul. 2017, pp. 1055–1056.
- [15] D. Kim and S. Kim, "Extrinsic parameter calibration of 2D radar-camera using point matching and generative optimization," in *Proc. 19th Int. Conf. Control, Autom. Syst. (ICCAS)*, Jeju, South Korea, Oct. 2019, pp. 99–103.
- [16] Y. Lihai, G. Jialong, J. Kai, and Y. Yanmei, "Research on synthetic aperture radar imaging characteristics of point targets," in *Proc. 2nd Asian-Pacific Conf. Synth. Aperture Radar*, Xi'an, China, Oct. 2009, pp. 282–285.
- [17] A. Algafsh, M. Inggs, and A. K. Mishra, "The effect of perforating the corner reflector on maximum radar cross section," in *Proc. 16th Medit. Microw. Symp. (MMS)*, Abu Dhabi, United Arab Emirates, Nov. 2016, pp. 1–4.
- [18] W.-B. Yim and W.-S. Kim, "Shaping analysis to decide the design condition of a passive-type radar reflector," *J. Korean Navigat. port Res.*, vol. 26, no. 2, pp. 199–207, Jun. 2002, doi: [10.5394/kinpr.2002.26.2.199](https://doi.org/10.5394/kinpr.2002.26.2.199).
- [19] L. C. Oldfield, "Radar cross section analysis and control. A. K. Bhattacharyya and D. L. Sengupta. Artech House, 6 Buckingham Gate, London, SW1E6JP. 1991. 289 pp. Illustrated. \$55.00." *Aeronaut. J.*, vol. 96, no. 952, p. 65, 1992, doi: [10.1017/S0001924000024568](https://doi.org/10.1017/S0001924000024568).
- [20] N. A. M. Daud, N. E. A. Rashid, K. A. Othman, and N. Ahmad, "Analysis on radar cross section of different target specifications for forward scatter radar (FSR)," in *Proc. 4th Int. Conf. Digit. Inf. Commun. Technol. its Appl. (DICTAP)*, Bangkok, Thailand, May 2014, pp. 353–356, doi: [10.1109/DICTAP.2014.6821710](https://doi.org/10.1109/DICTAP.2014.6821710).
- [21] J.-B. Yim and W.-S. Kim, "Design of passive-type radar reflector," *J. Navigat. Port Res.*, vol. 27, no. 3, pp. 267–272, Aug. 2003, doi: [10.5394/kinpr.2003.27.3.267](https://doi.org/10.5394/kinpr.2003.27.3.267).
- [22] J. Oh, K.-S. Kim, M. Park, and S. Kim, "A comparative study on camera-radar calibration methods," in *Proc. 15th Int. Conf. Control, Autom., Robot. Vis. (ICARCV)*, Singapore, Nov. 2018, pp. 1057–1062, doi: [10.1109/ICARCV.2018.8581329](https://doi.org/10.1109/ICARCV.2018.8581329).
- [23] G. Bradski, "The OpenCV library," *Dr. Dobb's J. Softw. Tools*, vol. 25, no. 11, pp. 1–120, 2000, Art. no. 123.
- [24] K. T. Olutomilayo, M. Bahramgiri, S. Nooshabadi, and D. R. Fuhrmann, "Extrinsic calibration of radar mount position and orientation with multiple target configurations," *IEEE Trans. Instrum. Meas.*, vol. 70, pp. 1–13, 2021.
- [25] J. Domhof, J. F. P. Kooij, and D. M. Gavrila, "An extrinsic calibration tool for radar, camera and LiDAR," in *Proc. Int. Conf. Robot. Autom. (ICRA)*, May 2019, pp. 8107–8113.
- [26] L. Cheng and S. Cao, "Online targetless radar-camera extrinsic calibration based on the common features of radar and camera," in *Proc. IEEE Nat. Aerosp. Electron. Conf. (NAECON)*. Piscataway, NJ, USA: Institute of Electrical and Electronics Engineers, Aug. 2023, pp. 294–299, doi: [10.1109/naecon58068.2023.10366051](https://doi.org/10.1109/naecon58068.2023.10366051).
- [27] J. H. Beattie, "The threat to the 'S' band marine radar frequency allocation and the necessity to preserve it," *J. Navigat.*, vol. 53, no. 2, pp. 299–312, May 2000, doi: [10.1017/s0373463300008791](https://doi.org/10.1017/s0373463300008791).
- [28] P. Virtanen et al., "SciPy 1.0: Fundamental algorithms for scientific computing in Python," *Nature Methods*, vol. 17, no. 3, pp. 261–272, Mar. 2020, doi: [10.1038/s41592-019-0686-2](https://doi.org/10.1038/s41592-019-0686-2).
- [29] TiHAN, IIT Hyderabad. *Technology Innovation Hub on Autonomous Navigation and Data Acquisition Systems*. [Online]. Available: <https://tihan.iith.ac.in/>
- [30] S. Song et al., "Research on time synchronization and spatial calibration algorithms of radar and camera," *J. Phys., Conf. Ser.*, vol. 2428, no. 1, Feb. 2023, Art. no. 012044, doi: [10.1088/1742-6596/2428/1/012044](https://doi.org/10.1088/1742-6596/2428/1/012044).
- [31] J. M. Lee et al., "Fine active calibration of camera position/orientation through pattern recognition," in *Proc. IEEE Int. Symp. Ind. Electron.*, vol. 2, Pretoria, South Africa, Jul. 1998, pp. 657–662, doi: [10.1109/ISIE.1998.711698](https://doi.org/10.1109/ISIE.1998.711698).
- [32] D. S. Pawar, P. A. Singh, and R. Pachamuthu, "Connected autonomous vehicles (CAV) testbed at IIT Hyderabad," in *Recent Trends in Transportation Infrastructure* (Lecture Notes in Civil Engineering), vol. 354, R. Rastogi, G. Bharath, D. Singh, Eds. Singapore: Springer, 2023.



Nitish Kumar (Graduate Student Member, IEEE) received the bachelor's degree in electronics and communication engineering from the Sri Siddhartha Institute of Technology, Tumkur, India, in 2019. He is currently pursuing the master's degree in communication and signal processing with the Department of Electrical Engineering, Indian Institute of Technology Hyderabad (IITH), Sangareddy, India.

His research areas include radar signal processing, radar-camera sensor fusion, wireless communication, and autonomous navigation.



Ayush Dasgupta received the B.Tech. degree in electronics and communication engineering from KL University, Hyderabad, India, in May 2024.

He has been working as a Junior Research Assistant Fellow at TiHAN, IIT Hyderabad. His research interests include the Internet of things, robotics, sensor networks, signal processing, and autonomous navigation.



Venkata Satyanand Mutnuri is currently the Technical Officer of the Technology Innovation Hub on Autonomous Navigation (TiHAN) Foundation, Indian Institute of Technology Hyderabad (IITH), Sangareddy, India. He has contributed to theoretical research on wave propagation analyses in vehicular structures and published over a dozen articles in journals and peer-reviewed conferences. His research areas include autonomous navigation of vehicles, camera/radar/light detection and ranging (LiDAR)/global navigation satellite system (GNSS)-based sensor data collection for Indian scenarios, safety envelopes, and control laws designed for aircraft.



Rajalakshmi Pachamuthu (Senior Member, IEEE) received the Ph.D. degree from Indian Institute of Technology (IIT) Madras, Chennai, India, in 2008.

She is currently a Professor with Indian Institute of Technology Hyderabad, Sangareddy, India. With more than 100 internationally reputed research publications, her research interests include the Internet of Things, artificial intelligence, cyber-physical systems, sensor networks, wireless networks, drone-based sensing, and light detection and ranging (LiDAR)-based traffic sensing.